CHAPTER 1

INTRODUCTION

1.1 Motive of Study

The complex vortex flow and associated thermal characteristics simultaneously driven by the buoyancy and inertia in a laminar convective gas jet impinging vertically downwards onto a heated horizontal disk confined in a vertical cylindrical chamber are directly relevant to the growth of single crystal thin films from the metal-organic chemical vapor deposition (MOCVD) processes in a vertical reactor and have been extensively investigated in the past decades [1]. The recent fast increase of the wafer size to reduce the fabrication cost needed in various microelectronic applications causes the buoyancy driven flow and heat transfer in MOCVD processes to become relatively complex and unstable. Vortex flow in the form of circular rolls has been unveiled. Depending on the jet Reynolds number and buoyancy-to-inertia ratio, up to four inertia-driven rolls and two buoyancy-driven rolls were observed in the impinging jet flow [2-4]. Besides, both the inertia- and buoyancy-driven time dependent vortex flows were identified. In spite of these findings, a more fundamental question on the low speed jet impinging onto a large heated disk considered here is the possible presence of other vortex flow patterns such as the radial rolls, bifurcation rolls, incomplete rolls, cells, etc. Under what conditions these new vortex rolls appear. This is still poorly understood and needs to be explored. In the present study numerical simulation is conducted to unravel the possible presence of new vortex flow structures and the associated flow and thermal

characteristics in a confined impinging air jet over a large horizontal heated disk. To simplify the numerical computation, the disk is not placed in a cylindrical chamber but the impinging jet is considered to be confined by an upper horizontal plate. Effects of the jet Reynolds number and Rayleigh number on the predicted flow and thermal structures will be examined in detail.

1.2 Literature Review

In a confined jet impingement flow over a large horizontal plate, we can identify three characteristic regions as schematically shown in Fig. 1.1. A potential core is formed which is called "the developing or free jet region" near the jet exit. Near the target plate, the jet impinges the plate and then is deflected away. We have the deflection zone of "the impingement flow region". Away from the stagnation point, the flow moves radially outwards called "the wall jet region". The literature relevant to the vortex flow and heat transfer in the jet impinging onto a heated plate is reviewed briefly in the following.

Considerable amount of work has been carried out in the past to study the fluid flow and heat transfer in the round or slot jet impinging vertically downwards onto a large horizontal plate without any confinement. Most of the studies focused on quantifying the highly efficient heat transfer and fluid flow associated with the high speed impinging jets. For instances, heat or mass transfer in the impinging jets over a large plate was experimentally investigated by Scholtz and Trass [5], Sparrow and Wong [6], Masliyah and Nguyen [7], and Hrycak [8]. Similar investigations on the cooling efficiency of the impinging jets were carried out by Chou et al. [9] and Chung and Luo [10]. Some recent numerical simulation predicted location of the centers of

inertia driven vortexes for liquid jet by the Reynolds stress model (Morris et al. [11, 12]). And effects of buoyancy on the flow field and heat transfer rate for aiding or opposing mixed convective impinging jets were investigated by Sarhini and Ruocco [13]. Heat transfer in laminar impinging jets with upper plate confinement was numerically predicted by Saad et al. [14] and Law and Masliyah [15]. A pair of big flow recirculations around the wall jet region in the form of circular vortex rolls were noted to result from the confinement plate (Chua et al. [16], Voke and Gao [17]). The characteristics of the recirculations were found to be influenced by the jet Reynolds number Re_j and nozzle-to-plate spacing H (Fitzgerald and Garimella [18], Park et al. [19], and Ichimiya [20]). Their numerical predictions revealed that the centers of the flow recirculations moved away from the jet axis and the recirculations were larger at increasing Re_j and H. Moreover, the secondary flow in a confined impinging jet includes a large recirculation roll vortex around the jet axis and a comparatively smaller neighboring vortex roll right above the impinging plate (Law and Masliyah [15, 21]). Details on the size and locations of the inertia driven primary and secondary vortex rolls affected by the Reynolds and Richardson numbers for laminar confined slot-jet (Re_j = 100 - 500) were recently examined by Sahoo and Sharif [22]. Moreover, for a confined laminar impinging jet (Re_j <1000) the critical jet Reynolds number for the onset of unsteady flow was numerically shown to be between 585 and 610 [23] and the breaking in the axisymmetric impinging jet structure began to appear at Re = 750 for H/W = 5. The unsteady jet was characterized by a dominant frequency corresponding to the formation of shear layer vortices at the jet exit. Critical reviews on impinging jets were conducted by Viskanta [24] and Jambunathan et al. [25]. A recent investigation from Santen et al. [26, 27] pointed out the onset of thermal instability for axisymmetric and three-dimensional vortexes. Besides, the secondary flow in the form of circular rolls, transverse (radial) rolls and three-dimensional

irregular rolls were mentioned. Moreover, the buoyancy induced secondary flow composed of regular torus-shaped rolls near the jet inlet is suppressed by the jet inertia. The three-dimensional irregular rolls appear in the region at larger radial distance from the jet axis because the buoyancy force dominates there. But the detailed characteristics of the transverse and irregular rolls were not investigated.

In the impinging jet flow confined in a chamber encountered in the chemical vapor deposition (CVD), the gases input to the CVD chamber are at relatively low flow rates and the wafer upon which thin crystal films are grown and processed is at an elevated temperature with the Reynolds and Rayleigh numbers respectively ranging from 1.0 to 100.0 and from 0 to 10^5 [1]. Under such circumstance the buoyancy in the flow is no longer small compared with the jet inertia. Significant flow recirculation can be induced by the combined effects of the inertia and buoyancy. The importance of the buoyancy on the recirculating flow in a vertical CVD reactor was demonstrated by Wahl [28]. Similar investigations have been carried out for various types of CVD reactors including the MOCVD [29-31] and organometallic vapor phase epitaxy (OMVPE) [32]. In these studies for the processing of the microelectronic circuits [28-33] various vortex flow patterns were reported in the jet impinging flow.

1.3 Objective of Present Study

The above literature review clearly reveals that in a jet impinging onto a heated disk the inertia and buoyancy driven vortex rolls aside from the circular rolls may be induced. But the patterns of these new vortex flows and the associated thermal characteristics remain largely explored. Numerical simulation will be conducted in the

4

present study to examine the possible presence of the inertia and buoyancy driven new vortex rolls in an air jet impinging onto a large heated disk with an upper plate confinement. Attention will be focused on delineating the conditions leading to the appearance of these rolls and the detailed flow characteristics of these rolls.
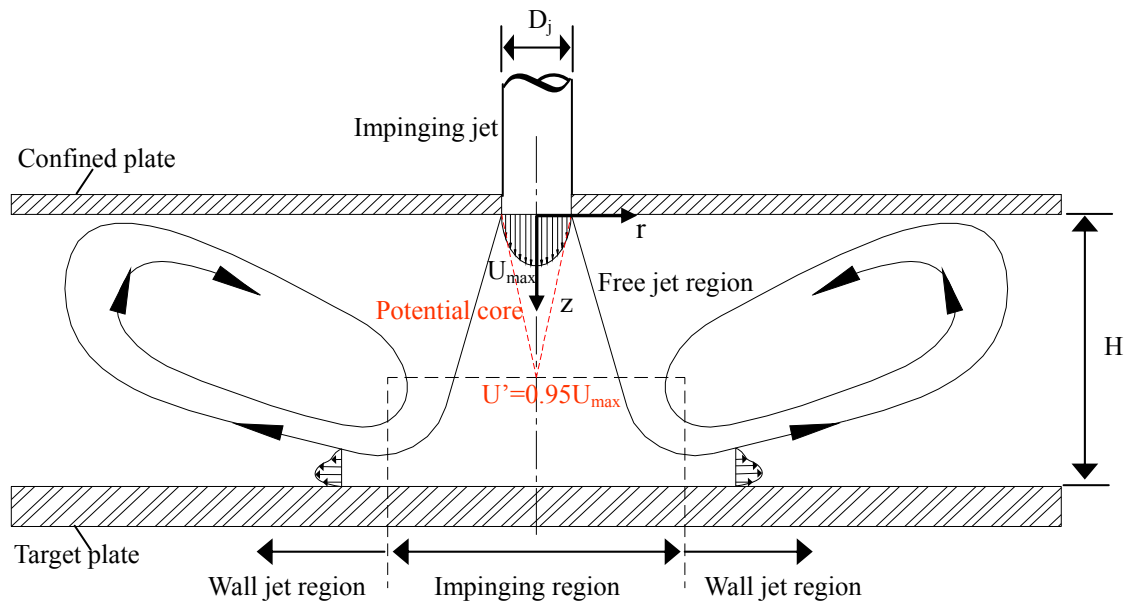
Fig. 1.1   Flow structure associated with a circular jet impinging onto a flat plate.

CHAPTER 2

MATHMATICAL FORMULATION

The physical model adopted here and the governing equations used to numerically predict the vortex flow patterns in the air jet impinging onto a large horizontal heated disk are described in this chapter.

2.1 Physical Model

The chosen physical model for the present vortex flow simulation of a confined impinging jet flow is shown in Fig. 2.1. Initially, the flow between the large heated disk and parallel confinement plate is stationary and isothermal at T_C. Then at time $t \geq 0$ an air jet is introduced from a long vertical circular injection pipe of uniform cross-section and injects vertically downwards onto the horizontal disk. At the inlet of the pipe the flow is assumed to be uniform at a speed V_i and at a uniform temperature T_C. Meanwhile, at time $t = 0$ we assume that the disk temperature is suddenly raised to a uniform value T_H and maintained at this level thereafter. In the mean time, the upper confinement plate is kept at a lower uniform temperature of T_C for $t \geq 0$. The temporal evolution of the flow following the jet impingement and the imposition of the temperature difference across heated disk and confinement plate is numerically predicted. In the percent simulation the injection pipe is chosen to be 600-mm long with 10.0 or 20.0 mm in diameter. The heated lower disk and cooled upper confinement plate are both 400.0 mm in diameter. Note that an annular insulated

7

section of 20.0 mm in length is attached to the edges of the upper and lower disks, intending to reduce the disturbances from the ambient of the jet flow. The ambient is assumed at a uniform temperature T_C.

2.2 Physical Assumptions and Governing Equations

To simplify the computation, the following assumptions are made:

(1) Flow is laminar and incompressible.

(2) Boussinesq approximation is valid and thermal radiation is neglected.

(3) Heat conduction in the wall of the injection pipe, confinement plate, and impingement plate are neglected in the computation. Besides, heat capacity effects associated with the pipe wall and the confinement and target plates are negligible.

(4) Neglect the viscous dissipation effect.

(5) $g_r = g_\theta = 0,\; g_z = -g$

Under these assumptions the basic equations describing the impinging jet flow are

Continuity equation-

$$\frac{1}{r}\frac{\partial}{\partial r}(ru) + \frac{1}{r}\frac{\partial}{\partial \theta}(v) + \frac{\partial}{\partial z}(w) = 0 \qquad (2.1)$$

r-momentum equation-

$$\rho\left[\frac{\partial u}{\partial t}+\left(u\frac{\partial}{\partial r}+\frac{1}{r}v\frac{\partial}{\partial \theta}+w\frac{\partial}{\partial z}\right)u-\frac{1}{r}v^2\right]$$
$$=-\frac{\partial p}{\partial r}+\mu\left[\frac{1}{r}\frac{\partial}{\partial r}\left(r\frac{\partial u}{\partial r}\right)+\frac{1}{r^2}\frac{\partial^2 u}{\partial \theta^2}+\frac{\partial^2 u}{\partial z^2}-\frac{u}{r^2}-\frac{2}{r^2}\frac{\partial v}{\partial \theta}\right] \qquad (2.2)$$

θ-momentum equation-

$$\rho\left[\frac{\partial v}{\partial t}+\left(u\frac{\partial}{\partial r}+\frac{1}{r}v\frac{\partial}{\partial \theta}+w\frac{\partial}{\partial z}\right)v+\frac{uv}{r}\right]$$
$$=-\frac{1}{r}\frac{\partial p}{\partial \theta}+\mu\left[\frac{1}{r}\frac{\partial}{\partial r}\left(r\frac{\partial v}{\partial r}\right)+\frac{1}{r^2}\frac{\partial^2 v}{\partial \theta^2}+\frac{\partial^2 v}{\partial z^2}+\frac{2}{r^2}\frac{\partial u}{\partial \theta}-\frac{v}{r^2}\right] \qquad (2.3)$$

z-momentum equation-

$$\rho\left[\frac{\partial w}{\partial t}+\left(u\frac{\partial}{\partial r}+\frac{1}{r}v\frac{\partial}{\partial \theta}+w\frac{\partial}{\partial z}\right)w\right]$$
$$=-\frac{\partial p}{\partial z}-\rho g+\mu\left[\frac{1}{r}\frac{\partial}{\partial r}\left(r\frac{\partial w}{\partial r}\right)+\frac{1}{r^2}\frac{\partial^2 w}{\partial \theta^2}+\frac{\partial^2 w}{\partial z^2}\right] \qquad (2.4)$$

Energy equation-

$$\rho c_p\left[\frac{\partial T}{\partial t}+u\frac{\partial T}{\partial r}+\frac{1}{r}v\frac{\partial T}{\partial \theta}+w\frac{\partial T}{\partial z}\right]=k\left[\frac{1}{r}\frac{\partial}{\partial r}\left(r\frac{\partial T}{\partial r}\right)+\frac{1}{r^2}\frac{\partial^2 T}{\partial \theta^2}+\frac{\partial^2 T}{\partial z^2}\right] \qquad (2.5)$$

The above equations are subjected to the following initial and boundary conditions:

For t < 0,

$$u = v = w = 0, T = T_C \qquad (2.6)$$

For t ≥ 0, at

Boundary I- Injection pipe inlet. At the injection pipe inlet the flow is uniform at T_c

$$u = v = 0, \ w = - V_j, \ T = T_C \text{ at } z = 600 \text{ mm};$$ (2.7)

Boundary II- Plate of confinement. At the upper confinement plate we have no-slip condition and $T = T_C$

$$u = v = w = 0, \ T = T_C \text{ at } z = 0;$$ (2.8)

Boundary III- Plate of impingement. At the lower heated disk $T=T_H$ and no-slip condition is also imposed

$$u = v = w = 0, \ T = T_H \text{ at } z = -H;$$ (2.9)

Boundary IV- Insulated annular section. At the upper and lower plates of the insulated annular section we also have no-slip condition and the plate are subjected to adiabatic condition

$$u = v = w = 0, \ \frac{\partial T}{\partial z} = 0 \text{ at } z = 0 \text{ and } -H \text{ for } \frac{D}{2} \leq r \leq \left(\frac{D}{2} + 20mm \right); \quad (2.10)$$

Boundary V- Outflow boundary. At the exit where the wall-jet flow leaves the insulated section the pressure and temperature are assumed at the ambient values. Besides, the redial gradient of the velocity is very small.

$$p = P_{amb}, \ T = T_C, \ \frac{\partial u}{\partial r} = \frac{\partial v}{\partial r} = \frac{\partial w}{\partial r} = 0 \text{ at } r = r_0.$$ (2.11)

These boundaries are specified in Fig. 2.2.

Using the nondimensional variables

$$\eta = \frac{r}{D_j} \qquad\qquad \phi = \theta \qquad\qquad \xi = \frac{z}{D_j}$$

$$U = \frac{u}{V_j} \qquad\qquad V = \frac{v}{V_j} \qquad\qquad W = \frac{w}{V_j}$$

$$P = \frac{P - P_{amb}}{\rho_o \cdot V_j{}^2} \qquad\qquad \Theta = \frac{T - T_C}{T_H - T_C} \qquad\qquad \Gamma = \frac{H}{D_j}$$

$$\mathrm{Pr} = \frac{v}{\alpha} \qquad\qquad Ra = \frac{g\beta(T_H - T_C)H^3}{\alpha v} \qquad\qquad \tau = \frac{t}{D_j / V_j}$$

and

$$\rho = \rho_o - \rho_o \beta(T - T_C)$$

$$T_o = \frac{T_H + T_C}{2}$$

The basic flow equations can be written in dimensionless form as

Continuity equation-

$$\frac{1}{\eta}\frac{\partial}{\partial \eta}(\eta U) + \frac{1}{\eta}\frac{\partial V}{\partial \phi} + \frac{\partial W}{\partial \xi} = 0 \qquad\qquad (2.12)$$

η-momentum equation-

$$\frac{\partial U}{\partial \tau} + U\frac{\partial U}{\partial \eta} + \frac{V}{\eta}\frac{\partial U}{\partial \phi} - \frac{V^2}{\eta} + W\frac{\partial U}{\partial \xi}$$
$$= -\frac{\partial P}{\partial \eta} + \frac{1}{\mathrm{Re}_j}\left\{ \frac{\partial}{\partial \eta}\left[\frac{1}{\eta}\frac{\partial}{\partial \eta}(\eta U)\right] + \frac{1}{\eta^2}\frac{\partial^2 U}{\partial \phi^2} - \frac{2}{\eta^2}\frac{\partial V}{\partial \phi} + \frac{\partial^2 U}{\partial \xi^2} \right\} \qquad (2.13)$$

ϕ-momentum equation-

$$\frac{\partial V}{\partial \tau} + U \frac{\partial V}{\partial \eta} + \frac{V}{\eta} \frac{\partial V}{\partial \phi} + \frac{UV}{\eta} + W \frac{\partial V}{\partial \xi}$$
$$= -\frac{1}{\eta} \frac{\partial P}{\partial \phi} + \frac{1}{\mathrm{Re}_j} \left\{ \frac{\partial}{\partial \eta} \left[\frac{1}{\eta} \frac{\partial}{\partial \eta} (\eta V) \right] + \frac{1}{\eta^2} \frac{\partial^2 V}{\partial \phi^2} + \frac{2}{\eta^2} \frac{\partial U}{\partial \phi} + \frac{\partial^2 U}{\partial \xi^2} \right\}$$
(2.14)

ξ-momentum equation-

$$\frac{\partial W}{\partial \tau} + U \frac{\partial W}{\partial \eta} + \frac{V}{\eta} \frac{\partial W}{\partial \phi} + W \frac{\partial W}{\partial \xi}$$
$$= -\frac{\partial P}{\partial \xi} + \frac{1}{\mathrm{Re}_j} \left\{ \frac{1}{\eta} \frac{\partial}{\partial \eta} \left(\eta \frac{\partial W}{\partial \eta} \right) + \frac{1}{\eta^2} \frac{\partial^2 W}{\partial \phi^2} + \frac{\partial^2 W}{\partial \xi^2} \right\} + \frac{1}{\left(\mathrm{Re}_j \right)^2 \cdot \Gamma^3} \cdot Ra \cdot \mathrm{Pr} \cdot \Theta$$
(2.15)

Energy equation-

$$\frac{\partial \Theta}{\partial \tau} + U \frac{\partial \Theta}{\partial \eta} + \frac{V}{\eta} \frac{\partial \Theta}{\partial \phi} + W \frac{\partial \Theta}{\partial \xi} = \frac{1}{\mathrm{Pr} \cdot \mathrm{Re}_j} \left\{ \frac{1}{\eta} \frac{\partial}{\partial \eta} \left(\eta \frac{\partial \Theta}{\partial \eta} \right) + \frac{1}{\eta^2} \frac{\partial^2 \Theta}{\partial \phi^2} + \frac{\partial^2 \Theta}{\partial \xi^2} \right\}$$ (2.16)

The above nondimensional governing equations are subjected to the following initial and boundary conditions:

For t < 0,

$$U = V = W = 0, \ \ \Theta = 0.$$ (2.17)

For t ≥ 0,

Boundary I- Injection pipe inlet. At the injection pipe inlet

$$U = V = 0, \ W = -1, \ \Theta = 0 \ \text{at} \ \ \xi = \frac{600}{D_j};$$ (2.18)

Boundary II- Plate of confinement. At the upper confinement plate

$$U = V = W = 0, \ \Theta = 0 \ \text{at} \ \xi = 0;$$ (2.19)

Boundary III- Plate of impingement. At the lower heated disk

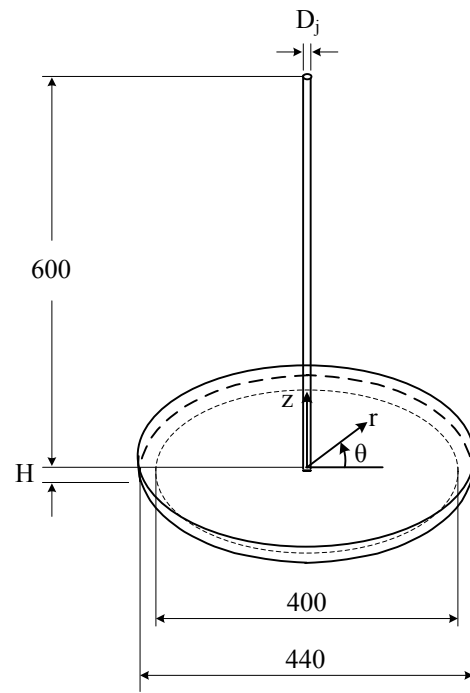$$U = V = W = 0, \ \Theta = 1 \ \text{ at } \ \xi = \frac{-H}{D_j} \ ; \qquad\qquad (2.20)$$

Boundary IV- Insulated annular section. At the upper and lower plates of the insulated annular section

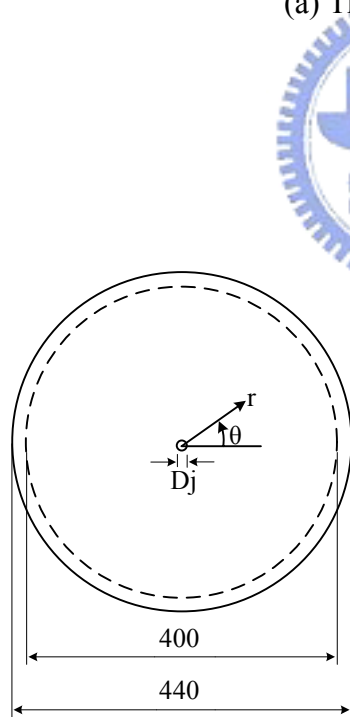$$U = V = W = 0, \ \frac{\partial \Theta}{\partial \xi} = 0 \ \text{ at } \ \xi = 0 \ \text{ and } \ \frac{-H}{D_j} \ ; \qquad\qquad (2.21)$$

Boundary V- Outflow boundary. At the exit of the wall-jet flow

$$P = 0, \ \Theta = 0 \ , \ \frac{\partial U}{\partial \eta} = \frac{\partial V}{\partial \eta} = \frac{\partial W}{\partial \eta} = 0 \ \text{ at } \ \eta = \frac{-r_0}{D_j} \ . \qquad\qquad (2.22)$$
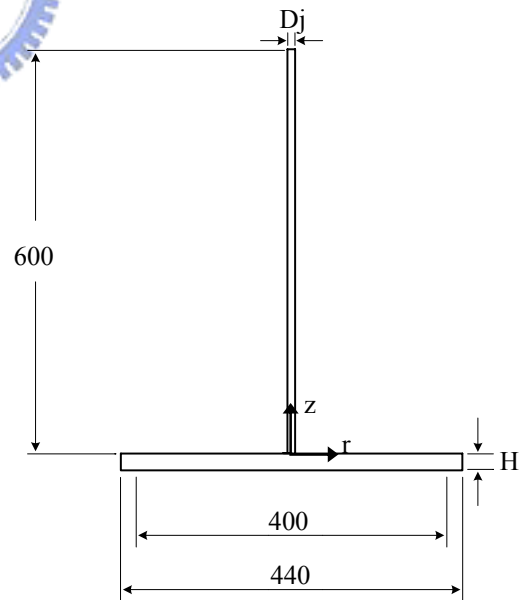

13

Fig. 2.1 Schematics illustrating the physical model for the typical case with $D_j =$ 10.0 mm and H = 20.0 mm from (a) three-dimensional view, (b) top view, and (c) side view. (unit: mm)
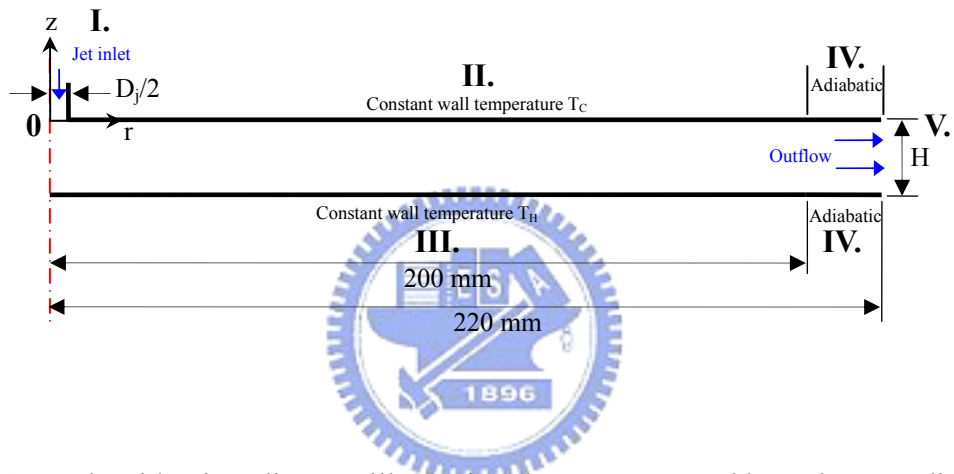
14

Fig. 2.2   The side view diagram illustrating the geometry and boundary conditions.